Inorganic Chemistry

pubs.acs.org/IC

Article

Coupling [Bmim]PF_6 and Pd NPs Modulated MOF-Based Material for Synergetic Regulating Electrocatalytic CO_2 Reduction

Peng Chen,[§] Yi-Rong Wang,[§] Hui Shui, Li-Ping Tang, Su-Hao Wu, Feng-Cui Shen,* and Ya-Qian Lan*

Cite This: https://doi.org/10.1021/acs.inorgchem.4c03960

Read Online

ACCESS | Metrics & More | Article Recommendations | Supporting Information

ABSTRACT: Metal−organic frameworks (MOFs) with a large number of active sites and high porosity are considered to be good platforms for the carbon dioxide electroreduction reaction (CO_2RR) but with confined low conductivity or low efficiency. Here, Pd-[Bmim]PF_6/Cu-BTC with exceptional selectivity and electron-transfer ability is elaborately designed by introducing ionic liquids (ILs) into the MOFs. ILs favor promoting the overall current density of the catalysts, and the introduction of Pd atoms combined with O atoms on the catalyst surface reconfigures into strong Pd−O bonds, improving the desorption efficiency of *CO. The unique structure of the catalyst Pd-[Bmim]PF_6/Cu-BTC leads to a significant improvement of the C_1 product with a high Faraday efficiency (FE) of 99.36%, especially for carbon monoxide (CO) with an FE of 93.18% (−1.1 V_{RHE}). The exceptional performance of the catalyst is verified by density functional theory (DFT) calculations, and the reduction of the free energy required by *HOCO as a key intermediate for CO production was only 0.12 eV, providing new insights to improve the electrocatalytic performance of MOF-based materials for the CO_2RR. In this research, an effective and promising strategy that configures active sites by larger current density is proposed to enhance the efficiency of the CO_2RR.

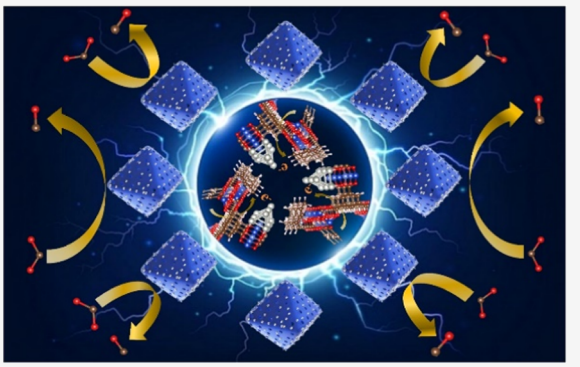

1. INTRODUCTION

Considering the urgency of developing and constructing a sustainable carbon-neutral strategy, the conversion of carbon dioxide into fuels and chemicals is one of the effective technological approaches to the utilization of carbon dioxide.[1,2] The emerging carbon dioxide electroreduction reaction (CO_2RR) powered by electricity generated from renewable energy sources has attracted much attention for its mild reaction conditions and considerable energy efficiency.[3,4] Currently, various industrial supplies, such as carbon monoxide (CO), formic acid, methane, ethylene, ethanol, etc., can be efficiently converted from CO_2RR by different electrocatalysts. In particular, CO is a promising product for industrial production as an important basis for C_1 chemistry for the synthesis of fine chemicals.[5] Various catalysts and nanostructures have been developed in the past decades to achieve efficient CO_2RR. Metal−organic framework-based (MOF-based) materials are ideal precatalysts because of their controllable size/shape, high surface area, chemical tunability, and open metal sites, providing a platform for the introduction of isolated active species among various alternatives.[6−13] Concurrently, increasing the charge-transfer capability of the catalytic sites in MOF-based materials improves the electrocatalytic activity and selectivity for CO_2RR.[14−16] The accurate structural information on MOF-based materials is conducive to elucidating the surface kinetic changes and chemisorption of the reaction intermediates. While MOF-based materials have several deficiencies that decrease the CO_2RR efficiency due to their poor electrical conductivity and slow electron transport rate, it is urgent to improve their conductivity and electron transport efficiency.[17−20]

Ionic liquids (ILs) with molten salt properties at room temperature consist entirely of cations and anions.[21] In particular, ILs are used as surface modifiers to modulate the catalytic performance of various electrocatalysts in the analysis of the CO_2RR pathway in different systems. The selectivity of ILs is also related to their ability to cooperate with CO_2RR intermediates.[22] ILs have been reported to reduce overpotentials and explicitly favor CO formation, possibly by coordinating with reducing intermediates (e.g., CO^{2-}), stabilizing the intermediates, or preventing their spatial proximity.[23] Additionally, ILs have excellent conductivity that is combined with various organic or inorganic carriers to design catalysts with large current density for CO_2RR owing to the stronger electron-transfer ability of the isomerization of the C_2 proton for the imidazolium cationic group in ILs driving by

Received: September 18, 2024
Revised: November 4, 2024
Accepted: November 7, 2024

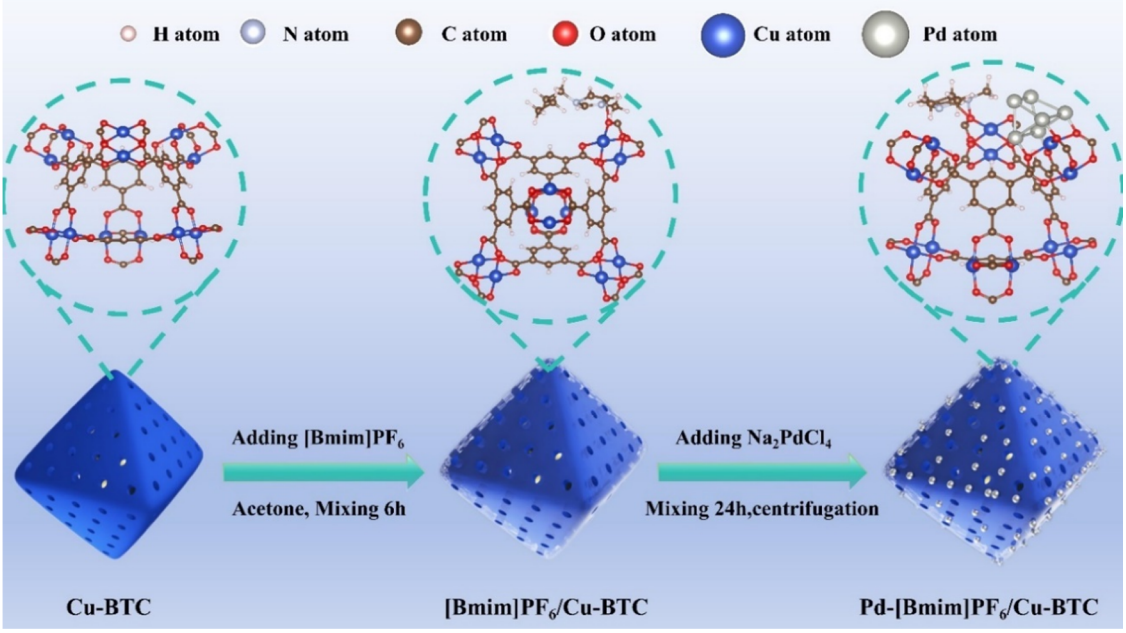

Figure 1. Schematic illustration of the synthetic process of the Pd-[Bmim]PF_6/Cu-BTC composite.

electrostatic/van der Waals interactions.[24] Concurrently, fluorine-containing anions absorb more CO_2 because of the stronger adsorption ability between F^- and the carbon atoms of CO_2 among the researched halogen anions.[25−27] Accordingly, the conversion of CO_2RR to CO is a slow kinetic process in which the production of *HOCO and the adsorption strength of *CO are the main factors governing CO production.[28−31]

Pd-based nanostructures, which are widely used in many electrochemical reactions, reveal excellent CO_2RR activity and selectivity to CO compared to other catalysts, thus attracting great interest from researchers for the structural evolution of catalysts and the reaction mechanisms behind the excellent catalytic performance.[32−35] Pd is converted to palladium hydride (PdH_1) upon binding in CO_2RR, which in turn improves CO conversion efficiency, making Pd as the potential electrochemical catalyst for CO_2 converted to CO.[36] Still, most palladium-based electrocatalysts face a fatal challenge of the generated CO strongly desorbing on the palladium surface and leading to rapid catalyst deactivation.[37,38] Introducing Pd into ionic liquid-functionalized MOFs would be an effective strategy to avoid deactivating Pd atoms, which is mainly attributed to Pd atoms bound to O atoms on the catalyst surface being reconfigured as a robust Pd−O bond to prevent the strong binding of Pd to *CO, which would have a favorable effect on the rate-limiting step and desorption process of *CO in the CO_2RR process, thus avoiding the deactivation of the catalyst in a short period of time.[39]

Hence, the excellent active site and pore properties of the MOF-based materials promote the CO_2RR and optimize the activation energy of *HOCO and *CO, while Cu-BTC displays a high desorption performance for CO_2. ILs favor the overall current density of the catalysts, and [Bmim]PF_6 also provides a fluorinated anionic environment, which prevents the occurrence of side reactions. In addition, the Pd−O bonds on the catalyst surface improve the desorption efficiency of *CO and accelerate the rate of electron migration in the catalyst, which results in a significant increase in the overall activation efficiency of the catalyst. As a result, the Pd-[Bmim]PF_6/Cu-BTC catalyst displays a carbon monoxide current density (j_{CO}) of −68.90 mA cm^{-2} at −1.1 V_{RHE}. The selectivity of the generated C_1 compounds is 99.36%; especially, the conversion faraday efficiency of CO reached 93.18% and still maintained superb electrochemical stability in 48 h. This will be attributed to the exquisite construction of the system, which endowed the Pd-[Bmim]PF_6/Cu-BTC catalyst with a high CO selectivity. This research will provide an enlightening strategy and insights for the design of highly CO-selective and robust MOF-based catalysts for large-scale CO_2RR.

2. EXPERIMENTAL SECTION

2.1. Synthesis of Cu-BTC. 0.25 M of $Cu(NO_3)_2{\cdot}3H_2O$ solution and 0.055 M of H_3BTC solution (water/ethanol = 1:2) were mixed uniformly and stirred for 10 min. The solution was transferred to Teflon-lined stainless autoclaves; then, the autoclaves were maintained at 110 °C for 24 h and cooled to room temperature naturally. The blue powder was washed thrice with DI water and ethanol and then dried at 60 °C in an oven.

2.2. Synthesis of [Bmim]PF_6/Cu-BTC. A 0.06 g portion of [Bmim]PF_6 and 0.075 g of Cu-BTC were mixed evenly in 7.5 mL of acetone and stirred for 6 h until the liquid in the beaker evaporated completely. Then, it was dried in an oven at 60 °C overnight.

2.3. Synthesis of Pd-[Bmim]PF_6/Cu-BTC Nanoparticle. A 0.09318 g amount of sodium tetrachloropalladate(II) was added to the beaker of [Bmim]PF_6/Cu-BTC as described above so that the molar ratio of Cu-BTC, [Bmim]PF_6, and Na_2PdCl_4 was 1:2:3, and 10 mL of distilled water was added and subsequently stirred for 24 h. The obtained composite Pd-[Bmim]PF_6/Cu-BTC nanoparticles were washed thrice with DI water and ethanol and then dried at 60 °C in an oven.

2.4. Synthesis of Reference Samples. Derived samples were prepared in the same way as the Pd-[Bmim]PF_6/Cu-BTC catalysts in the preparation of the working electrode, adjusting only the molar ratio of Cu-BTC, [Bmim]PF_6, and Na_2PdCl_4, the specific contents of which are shown in Table S1 and noted

https://doi.org/10.1021/acs.inorgchem.4c03960
Inorg. Chem. XXXX, XXX, XXX−XXX

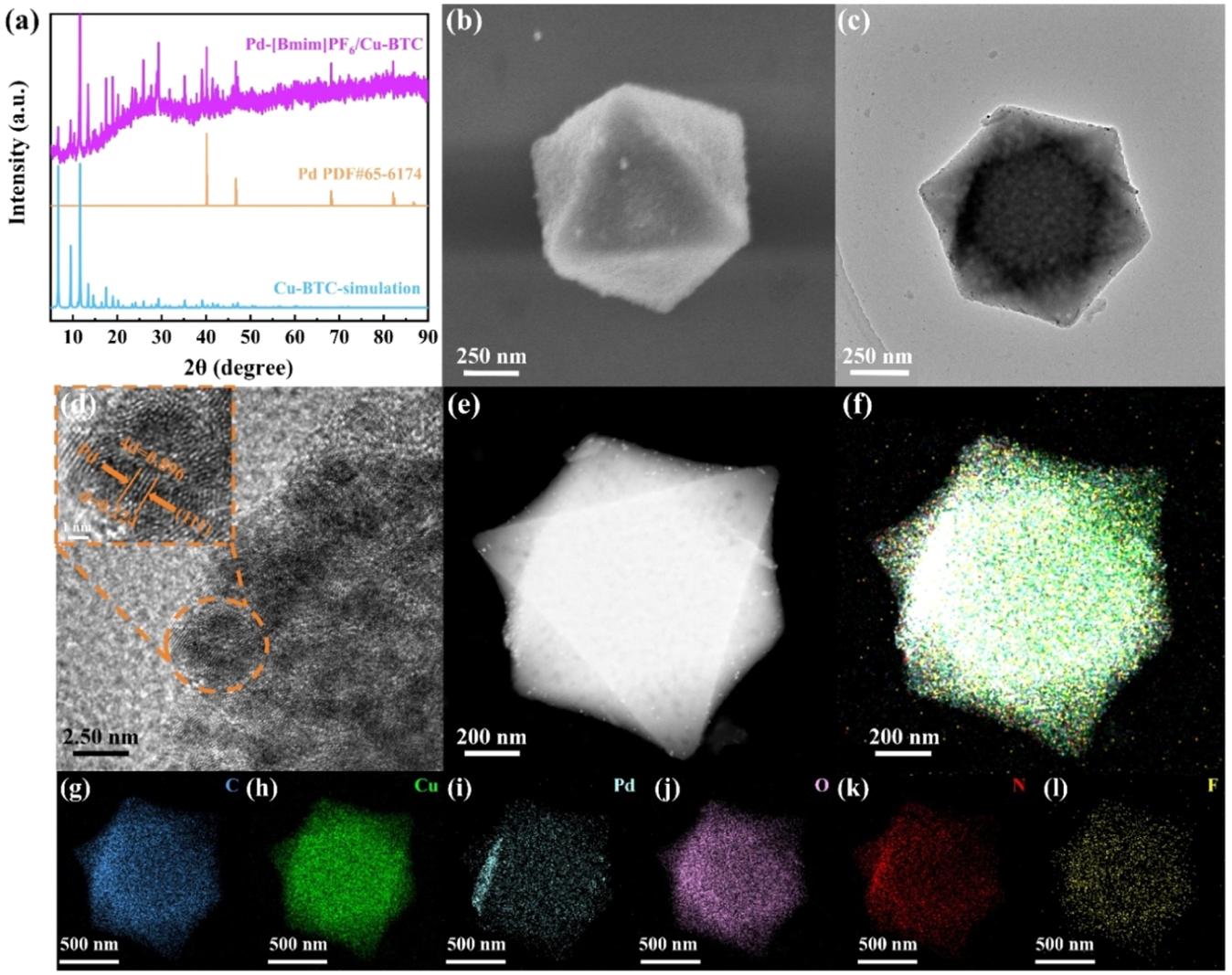

Figure 2. Electrochemical properties of the catalysts. (a) XRD patterns of the Pd-[Bmim]PF_6/Cu-BTC relative composites, (b) SEM images of Pd-[Bmim]PF_6/Cu-BTC nanospheres, (c) TEM images of Pd-[Bmim]PF_6/Cu-BTC, (d) HRTEM images of Pd-[Bmim]PF_6/Cu-BTC, and (e–l) HADDF and the corresponding EDX elemental mapping images of Pd-[Bmim]PF_6/Cu-BTC.

as Pd-[Bmim]PF_6/Cu-BTC-1 to −6, respectively. Meanwhile, the synthesis of Pd-[Bmim]PF_6/Co-BTC was similar to that of Pd-[Bmim]PF_6/Cu-BTC, with Co-BTC replacing Cu-BTC in the core. Pd-[Bmim]PO_4/Cu-BTC and Pd-DMPII/Cu-BTC were prepared using methods similar to those used for preparing Pd-[Bmim]PF_6/Cu-BTC by adding different ionic liquids [Bmim]PO_4 and DMPII, respectively, to the mixed solution.

2.5. Preparation of the Working Electrode. A 5 mg sample was dispersed in a solution containing 50 μL of Nafion solution (5 wt %), ethanol (250 μL), and water (200 μL) followed by 30 min of sonication. A 50 μL as-prepared catalyst ink was sprayed directly on a hydrophobic carbon paper (1 cm × 2 cm) to form a catalyst area of 0.5 × 1 cm^2. The catalyst deposited on the surface of the carbon paper was further dried at room temperature.

Additional descriptions of the experimental part are listed in the Supporting Information.

3. RESULTS AND DISCUSSION

3.1. Morphologies and Structure Analysis. The fabrication of the catalyst was revealed in Figure 1. The Cu-BTC was synthesized based on a previous report. First, [Bmim]PF_6/Cu-BTC was formed by attaching [Bmim]PF_6 on the surface of Cu-BTC, driven by valence bonding. Then, Pd-[Bmim]PF_6/Cu-BTC was acquired by adding Na_2PdCl_4 to [Bmim]PF_6/Cu-BTC, where [Bmim]PF_6 played multifunctional roles. On the one hand, highly conductive [Bmim]PF_6 enhanced the electron-transfer efficiency of the system facilitating multielectron transfer reactions for CO_2RR. On the other hand, [Bmim]PF_6 had a certain degree of reducibility, successfully reducing Pd^{2+} to Pd, which avoided the adverse effects on the catalyst caused by the addition of other reducing reagents in the reaction process.

The X-ray diffraction (XRD) patterns of the Pd-[Bmim]-PF_6/Cu-BTC sample were shown in Figure 2a. It exhibited main diffraction peaks (40.10, 46.72, 68.21, 82.12, and 86.73°) of crystalline Pd (PDF#65−6174), and simulated characteristic peaks (6.66, 10.42, 11.55, 13.43, and 18.93°) of Cu-BTC, indicating the successful synthesis of the catalysts. Furthermore, the catalyst displayed identical characteristic peaks and structures after IL modification (Figure S1a). XRD diffraction peaks also confirmed that Pd^{2+} was reduced to Pd nanoparticles (NPs) by different ILs in the Pd-[Bmim]PF_6/Co-

https://doi.org/10.1021/acs.inorgchem.4c03960
Inorg. Chem. XXXX, XXX, XXX−XXX

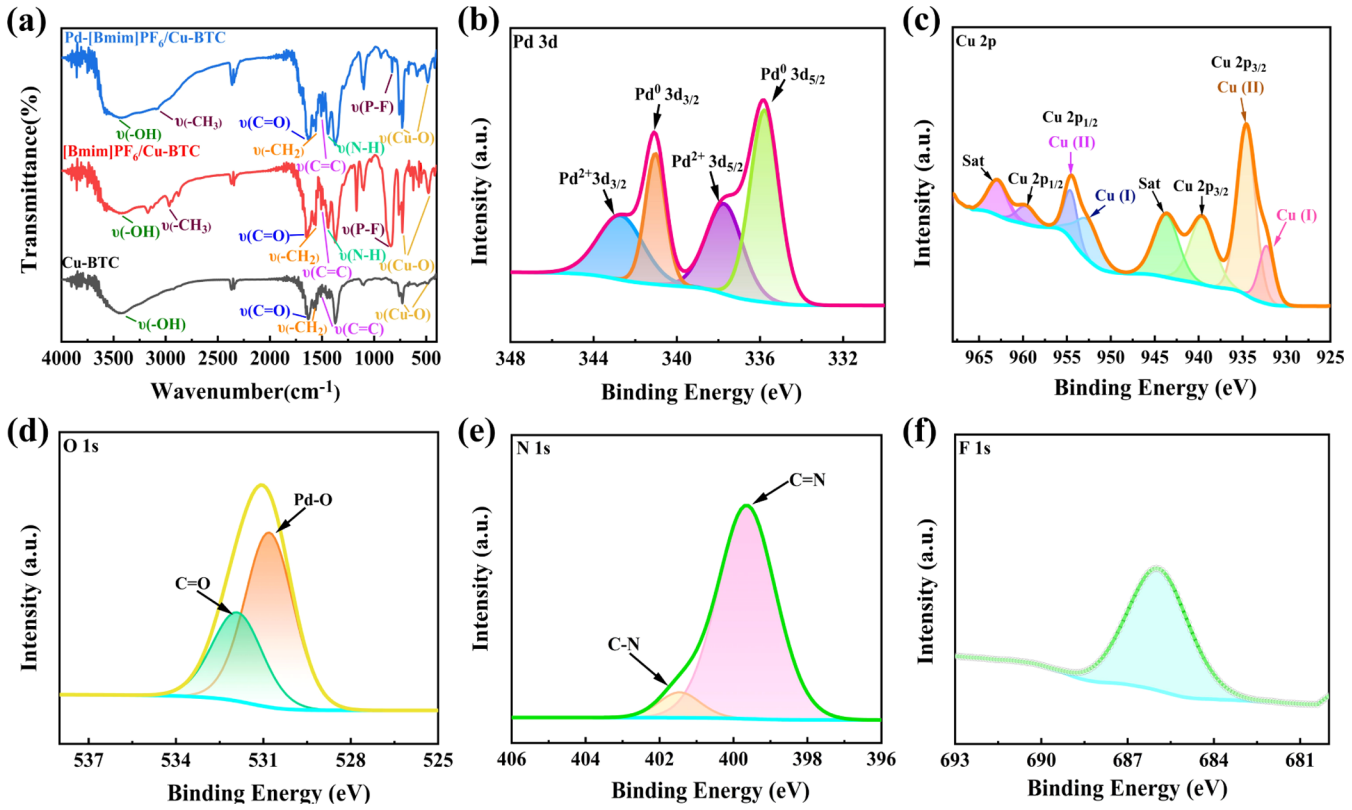

Figure 3. FT-IR and XPS of the electrocatalyst Pd-[Bmim]PF_6/Cu-BTC. (a) FT-IR spectra of Pd-[Bmim]PF_6/Cu-BTC. XPS spectra of (b) Pd 3d, (c) Cu 2p, (d) F 1s, (e) N 1s, and (f) O 1s.

BTC, Pd-[Bmim]PO_4/Cu-BTC, and Pd-DMPII/Cu-BTC catalysts (Figure S1b–d). Scanning electron microscopy (SEM) was accepted to analyze the surface morphology of Cu-BTC, [Bmim]PF_6/Cu-BTC, Pd-[Bmim]PO_4/Cu-BTC, Pd-DMPII/Cu-BTC, Co-BTC, Pd-[Bmim]PF_6/Co-BTC, and Pd-[Bmim]PF_6/Cu-BTC prepared as shown in Figures 2b and S2. The morphology of Cu-BTC can be clearly observed that the surface of the ortho-octahedral structure became rough after loading [Bmim]PF_6 (Figure S2a,b). Concurrently, the octahedral morphology of the Cu-BTC substrate remains unchanged after integrating with [Bmim]PF_6 and Na_2PdCl_4. The hexahedral size of the Pd-[Bmim]PF_6/Cu-BTC nanoparticles was about 0.75–1.25 μm. In addition, it was observed that the surfaces of Pd-[Bmim]PO_4/Cu-BTC and Pd-DMPII/Cu-BTC had different morphologies from the surface of Pd-[Bmim]PF_6/Cu-BTC ILs, and the Pd NPs appeared to be an aggregation phenomenon, thus having an effect on the proton transport rate of the electrolyte after replacing [Bmim]PF_6 with [Bmim]PO_4 and DMPII as shown in Figure S2c,d. Meanwhile, SEM images of Co-BTC showed that most of the spheres were in the size range of 0.75–1 μm (Figure S2e). And after the addition of [Bmim]PF_6 and Pd NPs, the Pd-[Bmim]PF_6/Co-BTC catalyst (Figure S2f) showed obvious agglomeration. The octahedral structure of Pd-[Bmim]PF_6/Cu-BTC was observed with NPs dispersing on the surface on the surface according to the transmission electron microscopy (TEM) in Figure 2c. High-resolution transmission electron microscopy (HRTEM) in Figure 2d displayed a lattice spacing of 0.224 nm corresponding to Pd NPs. Furthermore, elemental mapping images combined with the corresponding energy-dispersive X-ray spectra (EDS) and the high-angle annular dark-field (HADDF) (Figures 2e–l and S3) showed the presence of the Pd, F, Cu, C, N, and O elements in the Pd-[Bmim]PF_6/Cu-BTC catalysts, confirming the uniformly distributed elements.

Fourier transform infrared spectroscopy (FT-IR) data were analyzed to identify the successful incorporation of Pd NPs and [Bmim]PF_6 in Pd-[Bmim]PF_6/Cu-BTC (Figure 3a). The vibration bands at 728 and 489 cm^{-1} were attributed to the stretching vibration band of Cu–O.[40] Meanwhile, the absorption water peaks in the catalyst appeared in the spectral wavenumber range of 3046–3500 cm^{-1}, while two vibrational bands near 1540 and 3450 cm^{-1} are attributed to the C=C bonding asymmetry vibration and the –OH stretching vibration, respectively. In addition, the intensity of the C=O peak of the [Bmim]PF_6/Cu-BTC at 1650 cm^{-1} was significantly strengthened compared to that of Cu-BTC.[41] These data suggested that oxygen-containing functional groups were successfully introduced to the Cu-BTC surface. However, other new characteristic peaks were observed near 2970, 1570, 1465, and 842 cm^{-1} in the spectra of Pd-[Bmim]PF_6/Cu-BTC catalysts, representing $-CH_3$ and $-CH_2$ bonds in the alkane chain, N–H bonds in the imidazole ring, and P–F bond in the stretching vibration of PF_6^- bands, which were all derived from [Bmim]PF_6.[31] These results further indicated the successful preparation of catalysts Pd-[Bmim]PF_6/Cu-BTC. Besides, a comparison of the BET surface areas of Cu-BTC, [Bmim]PF_6/Cu-BTC, and Pd-[Bmim]PF_6/Cu-BTC is exhibited in Table S2. A low specific surface area of [Bmim]PF_6/Cu-BTC was due to clogging caused by ILs entering the MOF pores, whereas, the activity specific surface area of the Pd-[Bmim]PF_6/Cu-BTC catalyst increased under the action of partial ILs as reducing agents, which was favorable to the increase in the number of active sites with the promoted progress of three-

https://doi.org/10.1021/acs.inorgchem.4c03960
Inorg. Chem. XXXX, XXX, XXX–XXX

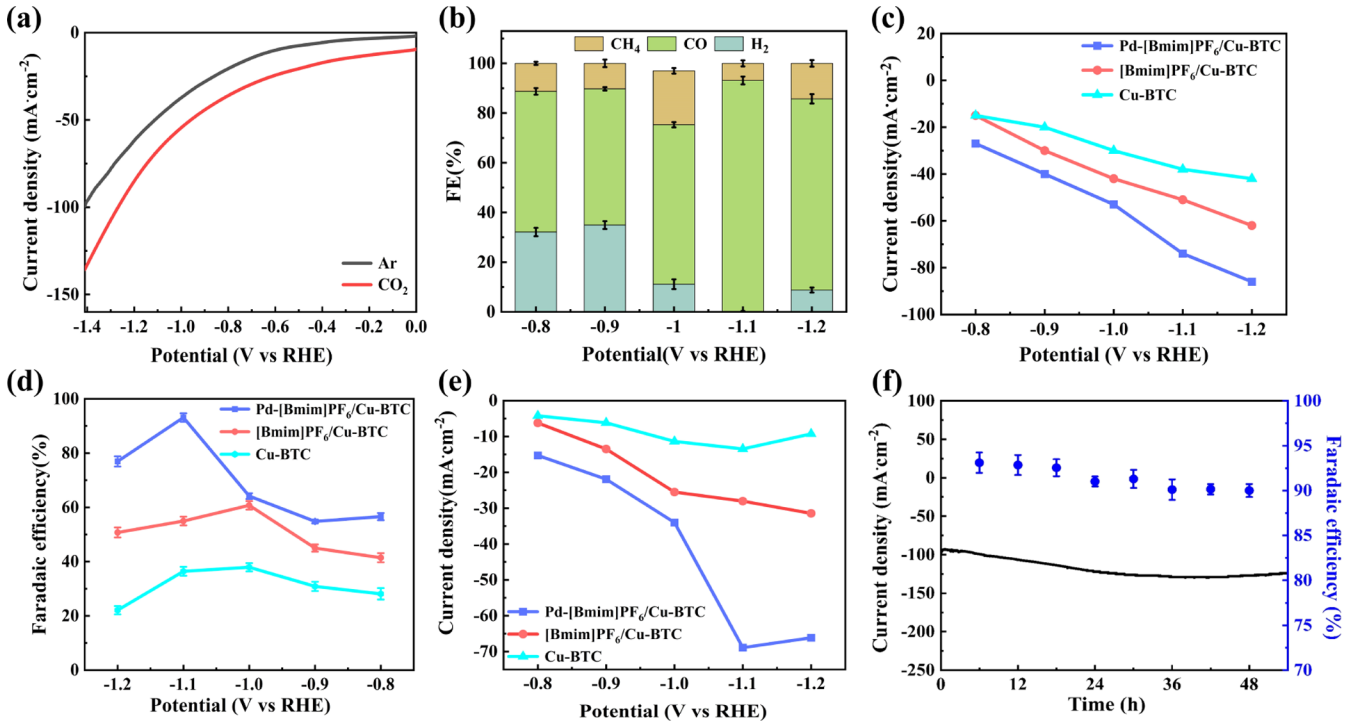

Figure 4. Electrochemical properties of catalysts in a flow cell. (a) LSV curves at a scan rate of 50 mV s^{-1} in Ar- and CO_2-saturated electrolytes, respectively, (b) the product distribution for CO_2RR at different potentials, (c) overall current density obtained for the catalyst at different applied potentials, (d) C_1 product selectivity on catalysts at different applied potentials, (e) j_{CO} obtained on catalysts at different applied potentials, and (f) FE_{CO} in the stability test at −1.1 V vs RHE.

phase reactions. The adsorption and desorption curves of nitrogen (N_2) showed that the adsorption capacity of N_2 by Pd-[Bmim]PF_6/Cu-BTC was higher than that of [Bmim]PF_6/Cu-BTC and Cu-BTC (Figure S4a,b), exhibiting the excellent adsorption performance of Pd-[Bmim]PF_6/Cu-BTC. The CO_2 adsorption and desorption characterizations were performed to evaluate the CO_2 adsorption capacity of Pd-[Bmim]PF_6/Cu-BTC. The CO_2 uptake capacities of Cu-BTC, [Bmim]PF_6/Cu-BTC, and Pd-[Bmim]PF_6/Cu-BTC at 273 K were 57.7425, 10.1976, and 72.6527 cm^3 g^{-1}, respectively (Figure S4c). The excellent working capacity of CO_2 by the Pd-[Bmim]PF_6/Cu-BTC catalyst offered convenience for the activation of CO_2 for the CO_2RR.

The composition and chemical states of the elements in Pd-[Bmim]PF_6/Cu-BTC were analyzed by using X-ray photoelectron spectroscopy (XPS). Characteristic peaks of elements C 1s, O 1s, Cu 2p, F 1s, N 1s, and Pd 3d were observed in the full spectrum analysis (Figure S5a). The C 1s spectrum emerged with two binding energies at 288 and 284.6 eV, corresponding to the O—C═O and C═C groups in the organic linker, respectively (Figure S5b). These strong feature peaks were acquired by the deconvolution of the Pd 3d spectrum belonging to Pd^0 $3d_{5/2}$ (335.79 eV) and Pd^0 $3d_{3/2}$ (341.04 eV), while the two weak shoulder peaks belonged to Pd^{2+} $3d_{5/2}$ (337.72 eV) or Pd^{2+} $3d_{3/2}$ (342.70 eV), respectively.[41,42] Notably, the appearance of the characteristic Pd^0 peaks also suggested the positive influence of [Bmim]PF_6 on the reduction of Pd^{2+} to Pd^0 NPs (Figure 3b). Simultaneously, the binding energies of Cu(I) $2p_{3/2}$ and Cu(I) $2p_{1/2}$ were 931.8 and 951.6 eV, respectively, which were consistent with those of Cu(I) (Figure 3c). Additionally, the 954.2 and 942.3 eV peaks and the 954.1 and 934.2 eV satellite peaks corresponded to Cu(II) $2p_{1/2}$ and Cu(II) $2p_{3/2}$, respectively.[19] For the XPS spectrum of O 1s (Figure 3d), the fitted two peaks of 530.8 and 531.9 eV were attributed to the lattice oxygen of the Pd−O and C═O bonds, respectively.[43] Likewise, there appeared two characteristic peaks in N 1s whose binding energies were displayed to be 284.6 and 288 eV for the C═N and C−N bonds (Figure 3e).[41,44] The characteristic peak binding energy of F 1s was 685.59 eV by XPS analysis (Figure 3f).[45]

3.2. CO_2RR Performance. The electrochemical CO_2RR performances of the catalysts were tested in a flow cell with different potentials. Linear scanning voltammetry (LSV) curves presented greater response currents in CO_2-saturated KOH solutions than in Ar-saturated solutions, validating the CO_2RR activity of Pd-[Bmim]PF_6/Cu-BTC (Figure 4a). Pd-[Bmim]-PF_6/Cu-BTC for the CO_2RR, gas chromatography (GC) and nuclear magnetic resonance (NMR) spectroscopic characterization were implemented to analyze the selectivity of the catalyst. The results revealed that H_2, CO, and CH_4 were the reduction products with a high Faraday efficiency (FE) without liquid products (Figure S6). CO was the major product with FE_{CO} of 93.18% in the gas-phase products during the CO_2RR of Pd-[Bmim]PF_6/Cu-BTC at a voltage of −1.1 V_{RHE}, and the $FE_{CO/CH4}$ of Pd-[Bmim]PF_6/Cu-BTC reached close to 100% (Figure 4b). Surprisingly, only a small amount of H_2 produced by the hydrogen evolution reaction (HER) was observed at a wide range of potentials (−0.8 and −1.2 V_{RHE}), demonstrating the low selectivity of Pd-[Bmim]PF_6/Cu-BTC for H_2. Comparatively, the FE_{CO} values of [Bmim]PF_6/Cu-BTC and Cu-BTC were only 60.76 and 37.92% (Figure S7), with FE_{H2} values as high as 41.63 and 73.13%, respectively. Furthermore, the current density of [Bmim]PF_6/Cu-BTC reached the overall current density of 51 mA·cm^{-2} at −1.1 V_{RHE}, which was 1.5 times of the current density of Cu-BTC (37 mA·cm^{-2})

https://doi.org/10.1021/acs.inorgchem.4c03960
Inorg. Chem. XXXX, XXX, XXX−XXX

and Pd-[Bmim]PF_6/Cu-BTC (74 mA·cm^{-2}) at −1.1 V_{RHE} (Figure 4c). A comparison of the FE_{CO} generation from catalysts Pd-[Bmim]PF_6/Cu-BTC, [Bmim]PF_6/Cu-BTC and Cu-BTC at different voltages was revealed in Figure 4d. The increasing current density of the Pd-[Bmim]PF_6/Cu-BTC catalyst displayed the accelerated rate of CO_2RR as the negative potential increased. While the j_{CO} of Pd-[Bmim]PF_6/Cu-BTC was much higher, the j_{CO} value showed a trend of Pd-[Bmim]PF_6/Cu-BTC>[Bmim]PF_6/Cu-BTC > Cu-BTC over the entire potential range of the CO_2RR, elaborating the contribution of Pd NPs and [Bmim]PF_6 for CO production. However, the j_{CO} values of Pd-[Bmim]PF_6/Cu-BTC (−68.90 mA cm^{-2}) were 2.45 and 5.1 times of [Bmim]PF_6/Cu-BTC (−28.02 mA cm^{-2}) and Cu-BTC (−13.47 mA cm^{-2}) at −1.1 V_{RHE} voltage, respectively (Figure 4e). Surprisingly, Pd-[Bmim]PF_6/Cu-BTC had the maximum FE_{CO} of 93.18% and j_{CO} of −68.90 mA cm^{-2} at −1.1 V_{RHE} voltage, which was even excellent for many Pd-based catalysts that appeared in the literature (Figure S8). The above results indicated that the elaborated construction of the catalyst Pd-[Bmim]PF_6/Cu-BTC was an excellent strategy to promote the targeted conversion of CO_2 into CO, which was mainly attributed to the fact that [Bmim]PF_6 played a good intermediate bridging role for the enhancement of the overall current density of the catalyst, the reducing agent transforming Pd^{2+} into Pd^0 and combining with the oxy-functional groups in the Cu-BTC to form Pd−O bonds.

The Pd-[Bmim]PF_6/Co-BTC catalyst was synthesized by substituting Co-BTC for Cu-BTC to elucidate the interaction between MOFs and electroreduction performance (Figure S9a). Most notably, Pd-[Bmim]PF_6/Co-BTC obtained the FE_{CO} of 71.67% for −1.1 V_{RHE} and a j_{CO} of 65.71 mA·cm^{-2}, and the overall performance was inferior to that of Pd-[Bmim]PF_6/Cu-BTC, inferring the significant impact of active sites of Cu-BTC on electrochemical performance. Besides, Cu-BTC and Pd, as active sites, were more likely to be associated with the interaction of halogen groups in different IL reaction carriers to promote the strong adsorption of CO_2 by the MOFs. When Pd-[Bmim]PO_4/Cu-BTC and Pd-DMPII/Cu-BTC were adopted as catalysts for the CO_2RR, FE_{CO} were 87.21 and 86.47% at −1.1 V_{RHE}, respectively. The selectivity of halogen-free ILs toward H_2 was slightly improved, and the j_{CO} is lower than that of halogen ILs in a wide voltage range, reflecting the role of halogen ion functional groups in the catalytic process (Figure S9b−d). The impacts of different molar ratios of components (Pd NPs, [Bmim]PF_6, and Cu-BTC) on the CO_2RR-efficient catalysts were also explored and labeled as Pd-[Bmim]PF_6/Cu-BTC −1 to −6, respectively (Table S1). The FE_{CO} and j_{CO} of Pd-[Bmim]PF_6/Cu-BTC displayed an increasing trend with the change of the molar ratio in the potential range from −0.8 to −1.2 V_{RHE}, reaching a maximum value at Pd/IL/Cu-BTC = 3:2:1 (Figures S10 and S11). These results suggested that the molar ratio of components in Pd-[Bmim]PF_6/Cu-BTC was crucial for the CO_2RR performance, with the predominance of Pd/IL/Cu-BTC at a molar ratio of 3:2:1 increasing the current density and effectively suppressing hydrogen generation. The number of catalytic active sites was explored to gain a deeper understanding of the reasons for the excellent electrochemical performance of the Pd-[Bmim]PF_6/Cu-BTC catalyst. To investigate the effective electrochemically active surface area (ECSA) of various catalysts during the CO_2RR, cyclic voltammetry (CV) with different scan rates was carried out to estimate the double-layer capacitance (C_{dl}) (Figures S12 and S13). The comparison of the C_{dl} values showed that Pd-[Bmim]PF_6/Cu-BTC had a better active specific surface area (6.39 mF cm^{-2}) than those of other catalysts. Therefore, Pd-[Bmim]PF_6/Cu-BTC exhibited the highest ECSA among the prepared electrocatalysts, which indicated that more active sites were exposed to boost the CO_2RR (Figure S14). The above data showed that the conjugates of the MOF-based material of Pd-[Bmim]PF_6/Cu-BTC could effectively increase the electrochemically active surface area and expose more accessible active sites to effectively boost catalysts' intrinsic activity.

The water droplet contact angles of Cu-BTC, [Bmim]PF_6/Cu-BTC, and Pd-[Bmim]PF_6/Cu-BTC were measured to investigate the wettability of catalysts (Figure S15). Cu-BTC crystals had a static water droplet contact angle of about 107° (Figure S15a), uniformly dispersing in the reaction medium, but the contact angle was only 14° (Figure S15b) in [Bmim]PF_6/Cu-BTC for the strong hydrophilicity of [Bmim]-PF_6. This was due to the increase of the number of oxygen-containing functional groups of [Bmim]PF_6/Cu-BTC. Notably, the hydrophobicity of the catalyst Pd-[Bmim]PF_6/Cu-BTC acquired a water droplet contact angle of 126° (Figure S15c), which implied that the introduction of the Pd active sites modulated the number of oxygen-containing functional groups of [Bmim]PF_6/Cu-BTC. The contact angle of Pd-[Bmim]PF_6/Cu-BTC after electrolysis was 115° (Figure S15d), demonstrating that the catalyst remained hydrophobic and protected the catalyst layer from flooding, which enables the catalyst layer to maintain a delicate balance between gas/liquid environments and creates a persistent three-phase interface for CO_2 electrolysis. Furthermore, the above observations indicate that hydrophobic catalysts dispersed in a reaction medium enhance a contact area between reactants with active compositions, thereby enhancing the conversion of reactants and ultimately affecting catalytic performance.[46] Charge-transfer resistance (R_{ct}) was also an important parameter used to assess the kinetics of catalytic reactions.[47,48] A lower resistance meant a faster rate of electron transfer and a smaller charge-transferred resistance of the interface between the electrolyte and the catalyst and can be obtained from the low-frequency region of the half-loop in the Nyquist diagram. EIS was used to study the charge-transfer capacity. The performance of catalysts is displayed in Figure S16 and Table S3. Pd-[Bmim]PF_6/Cu-BTC had a significantly smaller radius of the semicircle than those of the other electrocatalysts, which implied a smaller charge-transfer resistance and led to an increase in the CO_2RR activity. Obviously, Cu-BTC had a high resistance (136.76 Ω), but the merging of [Bmim]PF_6 and Pd NPs successfully decreased the resistance of the catalyst (38.64 Ω) and improved the charge-transfer efficiency, demonstrating its fast electron-transfer rate and reaction kinetics (Figure S17). We evaluated the long-term durability test utilizing a chronoamperometric curve at −1.1 V_{RHE} (Figure 4f) to analyze the electrochemical resistance of Pd-[Bmim]PF_6/Cu-BTC. The catalyst exhibited a small current decay and extraordinary stability over 48 h. Surprisingly, the FE_{CO} of the catalyst remained at 92.18% without a significant decrease. Concurrently, the CV cycling curves of the Pd-[Bmim]PF_6/Cu-BTC catalyst for 10,000 cycles were at a sweep speed of 100 mV/s with excellent stability (Figure S18). After the stability experiments, SEM, XRD, and IR analyses were carried out for Pd-[Bmim]PF_6/Cu-BTC (Figure S19). SEM images of

https://doi.org/10.1021/acs.inorgchem.4c03960
Inorg. Chem. XXXX, XXX, XXX−XXX

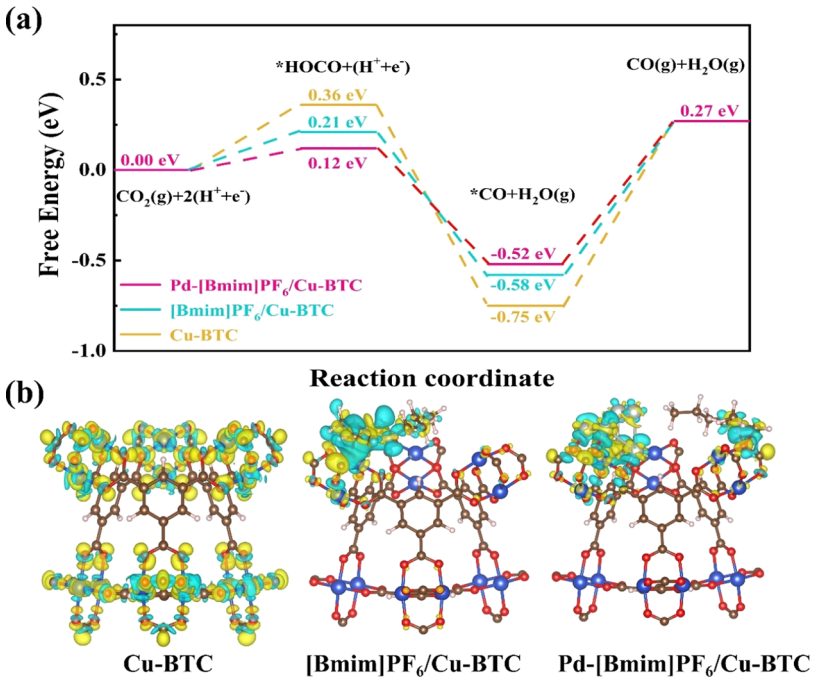

Figure 5. Mechanistic investigation of Pd-[Bmim]PF_6/Cu-BTC, [Bmim]PF_6/Cu-BTC, and Cu-BTC. ((a) DFT-calculated Gibbs free energy of the Pd-[Bmim]PF_6/Cu-BTC, [Bmim]PF_6/Cu-BTC, and Cu-BTC catalysts and b) differential charge density distribution of Pd-[Bmim]PF_6/Cu-BTC, [Bmim]PF_6/Cu-BTC, and Cu-BTC.

the catalysts after electrochemical testing (Figure S19a) found that the catalysts did not change their morphologies significantly before and after the reaction. Concurrently, the characteristic XRD (Figure S19b,c) peaks of this sample were crystalline Pd (40.10, 46.72, 68.21, 82.12, and 86.73°) and Cu-BTC (simulation) (6.66, 10.42, 11.55, 13.43, and 18.93°), the FT-IR images of the catalysts after electrochemical testing (Figure S19d) found that the Cu−O, P−F, and N−H characteristic peaks of the catalysts did not undergo significant changes before and after the reaction, exploding the Pd-[Bmim]PF_6/Cu-BTC catalyst's remarkable stability.

3.3. Theoretical Calculation. DFT calculations revealed the magnitude of the Gibbs free energy (Figure 5a) and the reaction pathways (Figure S20) of the Pd-[Bmim]PF_6/Cu-BTC, [Bmim]PF_6/Cu-BTC, and Cu-BTC catalysts for the conversion of CO_2 to CO, as well as the effect of the desorption strengths between the catalysts of CO_2RR. The surfaces of all three different catalysts promoted the activation energy of the *HOCO intermediate and reduced the desorption energy of CO_2 to produce CO in CO_2RR. Specifically, *HOCO formation was the key step that controlled the CO_2RR activity on MOF-based catalyst surfaces, with the Pd−O (0.12 eV) activation energy of the generated *HOCO for the reaction intermediates on the surface of Pd-[Bmim]PF_6/Cu-BTC being significantly lesser than that of Cu−O (0.36 eV) activation energy on the surface of Cu-BTC. At the same time, a much lower potential barrier was required for Pd to desorb the catalyst surface of *CO, avoiding CO poisoning and obscuring the active site. This suggested that the introduction of Pd modulated the electronic structure of Cu-BTC, lowering the overall potential energy barrier of the CO_2RR, which enhanced the desorption of *CO and improved the resistance ability of CO poisoning compared to that of Cu-BTC. More importantly, the differential charge density distributions of Pd-[Bmim]PF_6/Cu-BTC, [Bmim]PF_6/Cu-BTC, and Cu-BTC are revealed in Figure 5b, and strong interactions occurred on the Cu-BTC surface, resulting in a more significant accumulation effect on the electron density in the yellow region compared to that in the blue region. In particular, the electron density of Pd and the surrounding polarizing imidazole groups were mainly clustered on the Pd−O and C−O bonds imposed by strong coordination. This was mainly attributed to the polarized imidazolium group-reduced cation which acted as an initiator and reduced CO_2 to form an imidazolium−carbon dioxide adduct via a nucleophilic attack, which was followed by the transfer of the C_2 proton via an isomerization step. During electron transfer, the C_2 proton of the imidazolium cation interacted with the negatively charged $*CO_2^-$ formed on the Pd surface, highlighting the synergistic coupled electron−proton transfer mechanism. The charge density of Pd-[Bmim]PF_6/Cu-BTC catalysts was larger and more favorable for electron transport after loading with [Bmim]PF_6 and Pd, which enhanced the performance of CO_2RR. Thus, the interaction path from CO_2 to *HOCO to *CO was very favorable for the formation of CO products on the Pd-[Bmim]PF_6/Cu-BTC surface for the nucleophilic active site of deprotonation at the C_2 site of imidazole ILs and improved the selectivity of proton migration contributing to the high selectivity of the catalyst for generating CO.

4. CONCLUSIONS

In summary, a simple and effective MOF-based catalyst was designed by combining [Bmim]PF_6 and Pd NPs with Cu-BTC to improve the selectivity of CO in the CO_2RR. In particular, the composite Pd-[Bmim]PF_6/Cu-BTC showed an FE up to 99.36% for the constituent C_1 products, especially for CO (93.18%), besides excellent stability over 48 h. These excellent performances were attributed to the large surface area of Cu-BTC exposing abundant active sites and facilitating rapid electron transfer as well as [Bmim]PF_6 with the C_2 proton

https://doi.org/10.1021/acs.inorgchem.4c03960
Inorg. Chem. XXXX, XXX, XXX−XXX

isomerization and the excellent electrical conductivity. Furthermore, the introduction of Pd reduced the activation energy of the reaction intermediates and thus improved the reaction rate and CO selectivity. The Pd NPs interacted with ILs when binding to Cu-BTC to induce dynamic surface reconstruction and structural reorganization of the catalysts, which reduced the overall reaction potential of the catalysts and facilitated the regeneration of the activation sites. The research highlights effective strategies for the rational design of MOF-based catalyst electrocatalysts for the conversion of efficient CO_2RR into value-added chemicals.

■ ASSOCIATED CONTENT

Supporting Information

The Supporting Information is available free of charge at https://pubs.acs.org/doi/10.1021/acs.inorgchem.4c03960.

XRD pattern, SEM−EDS spectrum, XPS spectra, N_2 adsorption and desorption isotherms, 1H NMR spectra, CV curves, Faraday efficiency histogram, current density curves, Nyquist plot, and table of the BET surface area for all of the compounds; table of the main FE_{CO} catalytic performance of the catalysts synthesized in this work and table of R_{ct} values of different catalysts and onset potentials of samples (PDF)

■ AUTHOR INFORMATION

Corresponding Authors

Feng-Cui Shen − *School of Chemical and Environmental Engineering, Anhui Polytechnic University, Wuhu 241000, P. R. China;* orcid.org/0000-0002-7100-6261; Email: fcshen@ahpu.edu.cn

Ya-Qian Lan − *School of Chemistry, South China Normal University, Guangzhou 510006, P. R. China;* orcid.org/0000-0002-2140-7980; Email: yqlan@m.scnu.edu.cn

Authors

Peng Chen − *School of Chemical and Environmental Engineering, Anhui Polytechnic University, Wuhu 241000, P. R. China*

Yi-Rong Wang − *School of Chemistry, South China Normal University, Guangzhou 510006, P. R. China*

Hui Shui − *School of Chemical and Environmental Engineering, Anhui Polytechnic University, Wuhu 241000, P. R. China*

Li-Ping Tang − *School of Chemical and Environmental Engineering, Anhui Polytechnic University, Wuhu 241000, P. R. China*

Su-Hao Wu − *School of Chemical and Environmental Engineering, Anhui Polytechnic University, Wuhu 241000, P. R. China*

Complete contact information is available at: https://pubs.acs.org/10.1021/acs.inorgchem.4c03960

Author Contributions

[§]P.C. and Y.-R.W. contributed equally to this work.

Notes

The authors declare no competing financial interest.

■ ACKNOWLEDGMENTS

This work was financially supported by the National Natural Science Foundation of China (no. 21901003), the University Natural Science Research Project of Anhui Province (no. 2023AH040125), and the Anhui Province Action Plan for Cultivating Middle and Young Teachers (no. YQZD2023042). The authors also thank Keyangou Lab (www.sci-go.com) for the DFT calculation.

■ REFERENCES

(1) Xie, Z. H.; Huang, W.; Garg, S.; Hwang, S.; Liu, P.; Chen, J. G. G. CO_2 fixation into carbon nanofibres using electrochemical−thermochemical tandem catalysis. *Nat. Catal.* **2024**, *7*, 98−109.

(2) Ren, S. X.; Lees, E. W.; Hunt, C.; Jewlal, A.; Kim, Y. W.; Zhang, Z. S.; Mowbray, B. J. A. W.; Fink, A. G.; Melo, L.; Grant, E. R.; Berlinguette, C. P. Catalyst aggregation matters for immobilized molecular CO_2RR electrocatalysts. *J. Am. Chem. Soc.* **2023**, *145*, 4414−4420.

(3) Si, L. X.; Li, H.; Zhang, Y.; Zhang, D. H.; An, X. W.; Yao, M. M.; Shao, Y. Y.; Zhu, J.; Hu, S. Shape-dependence in seeded-growth of Pd-Cu solid solution from Pd nanostructure towards methanol oxidation electrocatalyst. *Nano Res.* **2023**, *16*, 9116−9124.

(4) Wagner, A.; Sahm, C. D.; Reisner, E. Towards molecular understanding of local chemical environment effects in electro- and photocatalytic CO_2 reduction. *Nat. Catal.* **2020**, *3*, 775−786.

(5) Jin, S.; Hao, Z.; Zhang, K.; Yan, Z.; Chen, J. Advances and challenges for the electrochemical reduction of CO_2 to CO: from fundamentals to industrialization. *Angew. Chem., Int. Ed.* **2021**, *60*, 20627−20648.

(6) Ifraemov, R.; Mukhopadhyay, S.; Hod, I. Photo-assisted electrochemical CO_2 reduction to CH_4 using a Co-porphyrin-based metal−organic framework. *Sol. RRL* **2023**, *7*, No. 2201068.

(7) Gao, Y.; Li, S. Z.; Gong, L.; Li, J.; Qi, D. D.; Liu, N. F.; Bian, Y. Z.; Jiang, J. Z. Unprecedented POSS-linked 3D covalent organic frameworks with scu or sqc topology regulated by porphyrin center for photocatalytic CO_2 reduction. *Angew. Chem., Int. Ed.* **2024**, *63*, 1208−1213.

(8) Gong, Y. N.; Mei, J. H.; Shi, W. J.; Liu, J. W.; Zhong, D. C.; Lu, T. B. Boosting CO_2 photoreduction to formate or CO with high selectivity over a covalent organic framework covalently anchored on graphene oxide. *Angew. Chem., Int. Ed.* **2024**, *63*, No. e202318735.

(9) Chu, Y. C.; Chen, K. H.; Tung, C. W.; Chen, H. C.; Wang, J.; Kuo, T. R.; Hsu, C. S.; Lin, K. H.; Li, D. T.; Chen, H. M. Dynamic (sub)surface-oxygen enables highly efficient carbonyl-coupling for electrochemical carbon dioxide reduction. *Adv. Mater.* **2024**, *36*, No. 2400640.

(10) Sengupta, D.; Melix, P.; Bose, S.; Duncan, J.; Wang, X. J.; Mian, M. R.; Kirlikovali, K. O.; Joodaki, F.; Islamoglu, T.; Yildirim, T.; Snurr, R. Q.; Farha, O. K. Air-stable Cu(I) metal−organic framework for hydrogen storage. *J. Am. Chem. Soc.* **2023**, *145*, 20492−20502.

(11) Li, Y.; Wang, H. H.; Yang, X. X.; Carroll, T.; Wu, G. Designing and engineering atomically dispersed metal catalysts for CO_2 to CO conversion: from single to dual metal sites. *Angew. Chem., Int. Ed.* **2024**, *63*, No. e202317884.

(12) Zhu, H.-J.; Si, D.-H.; Guo, H.; Chen, Z.; Cao, R.; Huang, Y.-B. Oxygen-tolerant CO_2 electroreduction over covalent organic frameworks via photoswitching control oxygen passivation strategy. *Nat. Commun.* **2024**, *15*, No. 1479.

(13) Liu, Y. Y.; Huang, J. R.; Zhu, H. L.; Liao, P. Q.; Chen, X. M. Simultaneous capture of CO_2 boosting its electroreduction in the micropores of a metal−organic framework. *Angew. Chem., Int. Ed.* **2023**, *62*, No. e202311265.

(14) Wu, Q.-J.; Si, D.-H.; Wu, Q.; Dong, Y.-L.; Cao, R.; Huang, Y.-B. Boosting Electroreduction of CO_2 over Cationic Covalent Organic Frameworks: Hydrogen Bonding Effects of Halogen Ions. *Angew. Chem., Int. Ed.* **2023**, *62*, No. e202215687.

(15) Huang, Z. W.; Hu, K. Q.; Li, X. B.; Bin, Z. N.; Wu, Q. Y.; Zhang, Z. H.; Guo, Z. J.; Wu, W. S.; Chai, Z. F.; Mei, L.; Shi, W. Q. Thermally induced orderly alignment of porphyrin photoactive motifs in metal−organic frameworks for boosting photocatalytic CO_2 reduction. *J. Am. Chem. Soc.* **2023**, *145*, 18148−18159.

(16) Wang, B.; Li, W.; Liu, Z.; Duan, Y.; Zhao, B.; Wang, Y.; Liu, J. Incorporating Ni-MOF structure with polypyrrole: enhanced capacitive behavior as electrode material for supercapacitor. *RSC Adv.* **2020**, *10*, 12129−12134.
(17) Lv, M.-H.; Cui, C.-X.; Huang, N.; Wu, M.-Z.; Wang, Q.; Gao, T.; Zheng, Y.; Li, H.; Liu, W.; Huang, Y.-P.; Ma, T.-Y.; Ye, L.-Q. Precisely Engineering Asymmetric Atomic CoN4 by Electron Donating and Extracting for Oxygen Reduction Reaction. *Angew. Chem., Int. Ed.* **2024**, *63*, No. e202315802.
(18) Liang, J. X.; Yu, H.; Shi, J. J.; Li, B.; Wu, L. X.; Wang, M. Dislocated bilayer MOF enables high-selectivity photocatalytic reduction of CO_2 to CO. *Adv. Mater.* **2023**, *35*, No. 2209814.
(19) Wen, Y.; Cheng, W.-H.; Wang, Y.-R.; Shen, F.-C.; Lan, Y.-Q. Tailoring the Hydrophobic Interface of Core−Shell HKUST-1@ Cu2O Nanocomposites for Efficiently Selective CO2 Electroreduction. *Small* **2023**, *16*, No. 2307467.
(20) Gong, Y. N.; Jiao, L.; Qian, Y.; Pan, C. Y.; Zheng, L.; Cai, X.; Liu, B.; Yu, S. H.; Jiang, H. L. Regulating the coordination environment of MOF-templated single-atom nickel electrocatalysts for boosting CO_2 reduction. *Angew. Chem., Int. Ed.* **2020**, *59*, 2705−2709.
(21) Rauber, D.; Philippi, F.; Schroeder, D.; Morgenstern, B.; White, A. J. P.; Jochum, M.; Welton, T.; Kay, C. W. M. Room temperature ionic liquids with two symmetric ions. *Chem. Sci.* **2023**, *14*, 10340−10346.
(22) El-Nagar, R. A.; Elaraby, A.; Nessim, M. I.; Ghanem, A. Designed imidazolium-based ionic liquids to capture carbon dioxide from natural gas. *J. Mol. Liq.* **2024**, *401*, No. 124708.
(23) Chen, S. Q.; Dong, Y. N.; Sun, J. J.; Gu, P.; Wang, J. F.; Zhang, S. J. Ionic liquids membranes for liquid separation: status and challenges. *Green Chem.* **2023**, *25*, 5813−5835.
(24) Starling, P. D. J.; Matilda, P. Influence of alkyl chain length of monocationic ionic liquids towards pharmacological activities. *J. Mol. Struct.* **2022**, *1251*, No. 132062.
(25) Rao, S. S.; Gejji, S. P. CO_2 Absorption using fluorine functionalized ionic liquids: interplay of hydrogen and sigma-hole interact. *J. Phys. Chem. A* **2016**, *120*, 1243−1260.
(26) Sistla, Y. S.; Sridhar, V. Molecular understanding of carbon dioxide interactions with ionic liquids. *J. Mol. Liq.* **2021**, *325*, No. 115162.
(27) Zhang, Z.; Zhang, L.; He, L.; Yuan, W.-L.; Xu, D.; Tao, G.-H. Is it always chemical when amino groups come across CO_2? anion-anion-interaction-induced inhibition of chemical adsorption. *J. Phys. Chem. B* **2019**, *123*, 6536−6542.
(28) Schellekens, M. P.; Raaijman, S. J.; Koper, M. T. M.; Corbett, P. J. Temperature-dependent selectivity for CO electroreduction on copper-based gas-diffusion electrodes at high current densities. *Chem. Eng. J.* **2024**, *483*, No. 149105.
(29) You, F.; Xi, S. B.; Ho, J. J. Y.; Calle-Vallejo, F.; Yeo, B. S. Influence of copper sites with different coordination on the adsorption and electroreduction of CO_2 and CO. *ACS Catal.* **2023**, *13*, 11136−11143.
(30) Meng, D. P.; Zheng, J. X.; Guo, J. X.; Gong, J. B.; Wang, Z. CuO-In_2O_3 collaboration in CO_2 electroreduction: Enhanced activity and synergistic mechanism. *Chem. Eng. J.* **2024**, *485*, No. 150051.
(31) Wang, P. P.; Zhu, J. M.; Tang, J. C.; Kang, J.; Shi, L. Morphology and CO_2 adsorption performance of novel ionic liquid microcapsules containing [Bmim][PF_6]. *Chem. Eng. Res. Des.* **2022**, *187*, 633−644.
(32) Gunji, T.; Ochiai, H.; Ohira, T.; Liu, Y.; Nakajima, Y.; Matsumoto, F. Preparation of various Pd-based alloys for electrocatalytic CO_2 reduction reaction—selectivity depending on secondary elements. *Chem. Mater.* **2020**, *32*, 6855−6863.
(33) Wu, X. H.; Guo, Y. N.; Sun, Z. S.; Xie, F. H.; Guan, D. Q.; Dai, J.; Yu, F. J.; Hu, Z. W.; Huang, Y. C.; Pao, C. W.; Chen, J. L.; Zhou, W.; Shao, Z. P. Fast operando spectroscopy tracking in situ generation of rich defects in silver nanocrystals for highly selective electrochemical CO_2 reduction. *Nat. Commun.* **2021**, *12*, No. 660.
(34) Bok, J.; Lee, S. Y.; Lee, B. H.; Kim, C.; Nguyen, D. L. T.; Kim, J. W.; Jung, E.; Lee, C. W.; Jung, Y.; Lee, H. S.; Kim, J.; Lee, K.; Ko, W.; Kim, Y. S.; Cho, S.-P.; Yoo, J. S.; Hyeon, T.; Hwang, Y. J. Designing atomically dispersed au on tensile-strained Pd for efficient CO_2 electroreduction to formate. *J. Am. Chem. Soc.* **2021**, *143*, 5386−5395.
(35) Zhang, N.; Zhang, X.; Kang, Y.; Ye, C.; Jin, R.; Yan, H.; Lin, R.; Yang, J.; Xu, Q.; Wang, Y.; Zhang, Q.; Gu, L.; Liu, L.; Song, W.; Liu, J.; Wang, D.; Li, Y. Supported Pd_2 dual-atom site catalyst for efficient electrochemical CO_2 reduction. *Angew. Chem., Int. Ed.* **2021**, *60*, 13388−13393.
(36) Chang, Q. W.; Kim, J.; Lee, J. H.; Kattel, S.; Chen, J. G.; Choi, S. I.; Chen, Z. Boosting activity and selectivity of CO_2 electroreduction by pre-hybridizing Pd nanocubes. *Small* **2020**, *23*, No. 2005305.
(37) Zito, A. M.; Clarke, L. E.; Barlow, J. M.; Bím, D.; Zhang, Z. S.; Ripley, K. M.; Li, C. J.; Kummeth, A.; Leonard, M. E.; Alexandrova, A. N.; Brushett, F. R.; Yang, J. Y. Electrochemical carbon dioxide capture and concentration. *Chem. Rev.* **2023**, *123*, 8069−8098.
(38) Chatterjee, S.; Griego, C.; Hart, J. L.; Li, Y.; Taheri, M. L.; Keith, J.; Snyder, J. D. Free standing nanoporous palladium alloys as CO poisoning tolerant electrocatalysts for the electrochemical reduction of CO_2 to formate. *ACS Catal.* **2019**, *9*, 5290−5301.
(39) Tan, X. Y.; Yu, C.; Song, X. D.; Ni, L.; Xu, H. Y.; Xie, Y. Y.; Wang, Z.; Cui, S.; Ren, Y. W.; Li, W. B.; Zhang, Y. F.; Qiu, J. S. Robust O-Pd-Cl catalyst-electrolyte interfaces enhance CO tolerance of Pd/ C catalyst for stable CO_2 electroreduction. *Nano Energy* **2022**, *104*, No. 107957.
(40) Alhumaimess, M. S.; Essawy, A. A.; Kamel, M. M.; Alsohaimi, I. H.; Hassan, H. M. A. Biogenic-mediated synthesis of mesoporous Cu_2O/CuO nano-architectures of superior catalytic reductive towards nitroaromatics. *Nanomaterials* **2020**, *10*, No. 781.
(41) Wu, L.; Qin, H.; Zhou, S. H.; Luo, Z. M.; Xiao, Y.; You, H.; Lin, Q.; Pan, H. Y.; Wang, K. L. Electronic regulation and hydrophobicity improvement of the palladium active site by ionic liquid to achieve high selectivity direct synthesis of hydrogen peroxide. *Chem. Eng. J.* **2023**, *474*, No. 145829.
(42) Ji, X.; Chen, D.; Peng, L.; Frison, F.; Valle, C. D.; Tubaro, C.; et al. Sustainable direct H_2O_2 synthesis over Pd catalyst supported on mesoporous carbon: The effect of surface nitrogen functionality. *Catal. Today.* **2021**, *376*, 1−8.
(43) Lv, J.; Wu, S.; Tian, Z.; Ye, Y.; Liu, J.; Liang, C. Construction of PdO-Pd interfaces assisted by laser irradiation for enhanced electrocatalytic N_2 reduction reaction. *J. Mater. Chem. A* **2019**, *7*, 12627−12634.
(44) Yoon, J.; Han, G.; Lee, M. W.; Lee, S.; Lee, S. H.; Lee, K. Amine functionalization derived lattice engineered and electron deficient palladium catalyst for selective production of hydrogen peroxide. *Appl. Surf. Sci.* **2022**, *604*, No. 154464.
(45) Yang, T.; Yang, C.; Le, J.; Yu, Z.; Bu, L.; Li, L.; Bai, S.; Shao, Qi.; Hu, Z.; Pao, C.-W.; Cheng, J.; Feng, Y.; Huang, X. Atomically isolated Pd sites within Pd-S nanocrystals enable trifunctional catalysis for direct, electrocatalytic and photocatalytic syntheses of H_2O_2. *Nano Res.* **2022**, *15* (3), 1861−1867.
(46) You, H.; Fu, C.; Wang, M.; Yang, C.; Shi, Y.; Pan, H.; Lin, Q. Pd/CNT with controllable Pd particle size and hydrophilicity for improved direct synthesis efficiency of H_2O_2. *New J. Chem.* **2022**, *46*, 12093−12102.
(47) Abdellah, A. M.; Ismail, F.; Siig, O. W.; Yang, J.; Andrei, C. M.; DiCecco, L.A.; Rakhsha, A.; Salem, K. E.; Grandfield, K.; Bassim, N.; Black, R.; Kastlunger, G.; Soleymani, L.; Higgins, D. Impact of palladium/palladium hydride conversion on electrochemical CO_2 reduction via in-situ transmission electron microscopy and diffraction. *Nat. Commun.* **2024**, *15*, No. 938.
(48) Liu, Y. M.; Tian, D.; Biswas, A. N.; Xie, Z. H.; Hwang, S.; Lee, J. H.; Meng, H.; Chen, J. G. G. Transition metal nitrides as novel catalyst supports for tuning CO/H_2 syngas production from electrochemical CO_2 reduction. *Angew. Chem., Int. Ed.* **2020**, *59*, 11345−11348.

https://doi.org/10.1021/acs.inorgchem.4c03960
Inorg. Chem. XXXX, XXX, XXX−XXX